Supplementary Information

Interfacial excitons across dimensional boundaries: mixed-dimensional SnS/BNNT heterostructure

Dhanjit Talukdar,[*,a] Dambarudhar Mohanta,[b] and Gazi A. Ahmed[a]

[a]*Optoelectronics and Photonics Laboratory, Department of Physics, Tezpur University, Napaam 784028, Assam, India*

[b]*Nanoscience and Soft-Matter Laboratory, Department of Physics, Tezpur University, Napaam 784028, Assam, India*

**Author to whom correspondence should be addressed: talukdardhanjit123@gmail.com, dhanjit@tezu.ernet.in*

S1. Computational details

The calculations are done using the PWSCF code in the Quantum Espresso software suite based on DFT and plane-wave pseudopotential approach.[1–4] The generalized-gradient-approximation (GGA) with non-empirical Perdew-Burke-Ernzerhof (PBE) parameterization is used to treat the exchange-correlation functional in the calculations.[5] The electron-ion interactions are modelled using the scalar-relativistic Optimized Norm-Conserving Vanderbilt Pseudopotential (ONCVPSP).[6] The kinetic energy cutoff (ecutwfc) and the charge density cutoff (ecutrho) for the wavefunctions is kept at 50 Ry, and 300 Ry, respectively. The sampling of the primary Brillouin zone (BZ) for BNNT, monolayer SnS, SnS/BNNT heterostructures are done at 1×6×1, 6×6×1, 6×6×1 *k*-point grid, respectively generated via the Monkhorst-Pack scheme. For a precise integration of the BZ during the non-self-consistent calculations, an even denser corresponding *k*-grid of 1×18×1, 12×12×1, 12×12×1, are considered for the three structures respectively. An energy convergence threshold of 10^{-4} Ry and a force convergence threshold of 10^{-3} Ry/Bohr are used to relax the lattice and atomic parameters. The convergence criteria for self-consistent calculation are set at 10^{-8} Ry. Semi-empirical Grimme's DFT-D2 parameter accounts for the vdW force in the heterostructure.[7]

Lattice mismatch along the direction of the nanotube axis is calculated by,

$$\frac{L_{SnS}-L_{BNNT}}{L_{SnS}} \times 100 \quad \ldots(1)$$

here, L_{SnS} and L_{BNNT} are the lattice parameters of SnS supercell and BNNT unit cell along *y*-direction.

The interface binding energy (E_b) per unit cell of the heterostructure is calculated by the following formula:

$$E_{\mathrm{b}} = E_{\mathrm{SnS/BNNT}} - E_{\mathrm{SnS}} - E_{\mathrm{BNNT}} \quad \ldots(2)$$

the terms $E_{\mathrm{SnS/BNNT}}$, E_{SnS}, E_{BNNT} represent the total energies of the SnS/BNNT heterostructure, isolated SnS layer, and BNNT, respectively.

The equation to calculate the charge density difference (CDD) is as follows:

$$\triangle \rho = \rho_{\mathrm{SnS/BNNT}} - \rho_{\mathrm{SnS}} - \rho_{\mathrm{BNNT}} \quad \ldots(3)$$

where, $\rho_{\mathrm{SnS/BNNT}}$, ρ_{SnS}, ρ_{BNNT} indicate the overall charge densities of the SnS/BNNT heterostructure, isolated SnS layer, and BNNT, respectively.

Beyond DFT, the energy levels are corrected by introducing quasiparticle interactions through GW computations based on MBPT. The quasiparticle interaction is introduced by the following non-linear equation,

$$E_{nk}^{QP} = \epsilon_{nk} + Z_{nk} < \Psi_{nk} | \Sigma\left(E_{nk}^{QP}\right) - V_{xc} | \Psi_{nk} > \quad \ldots(4)$$

where the term Z_{nk} represents renormalisation factor. With the evaluation of the dynamical and static components in the self-energy (Σ), the plasmon-pole approximation (PPA) is used to determine the single pole function frequency subjected to the dielectric matrix.[8,9]

The excitonic electron-hole effect is incorporated by solving the Bethe-Salpeter Equation (BSE) [9,10],

$$(E_{ck} - E_{vk}) A_{vck}^{S} + \sum_{kv'c'} < vck | K^{eh} | v'c'k' > A_{v'c'k'}^{S} = \Omega^{s} A_{vck}^{S} \quad \ldots(5)$$

where, the screened interaction between excited electrons and holes are described by the kernel term K^{eh}.[9,10] The terms A_{vck}^{S}, and Ω^{s} represent the electron-hole amplitudes, and the exciton energy, respectively. E_{ck} and E_{vk} are the quasiparticle energies of the electron and hole states. The subscripts v, c, and k represents the valence band (VB), conduction band (CB), and k vector, respectively. The GW+BSE computation is done using the YAMBO package.[11,12]

The number of bands used to construct the RPA response function for the SnS/(5,0), SnS/(6,0), and SnS/(7,0) BNNT heterostructures were set to 180, 200, and 200, respectively. The dielectric matrix ($\varepsilon^{-1}_{G,G'}$) was expanded using four energy blocks (4 Ry cutoff) for all

heterostructures. Similarly, the number of unoccupied states included in the correlation self-energy summation were 180, 200, and 200 for SnS/(5,0), SnS/(6,0), and SnS/(7,0) BNNT, respectively. The convergence tests for these parameters are presented in Figs. S1–S3.

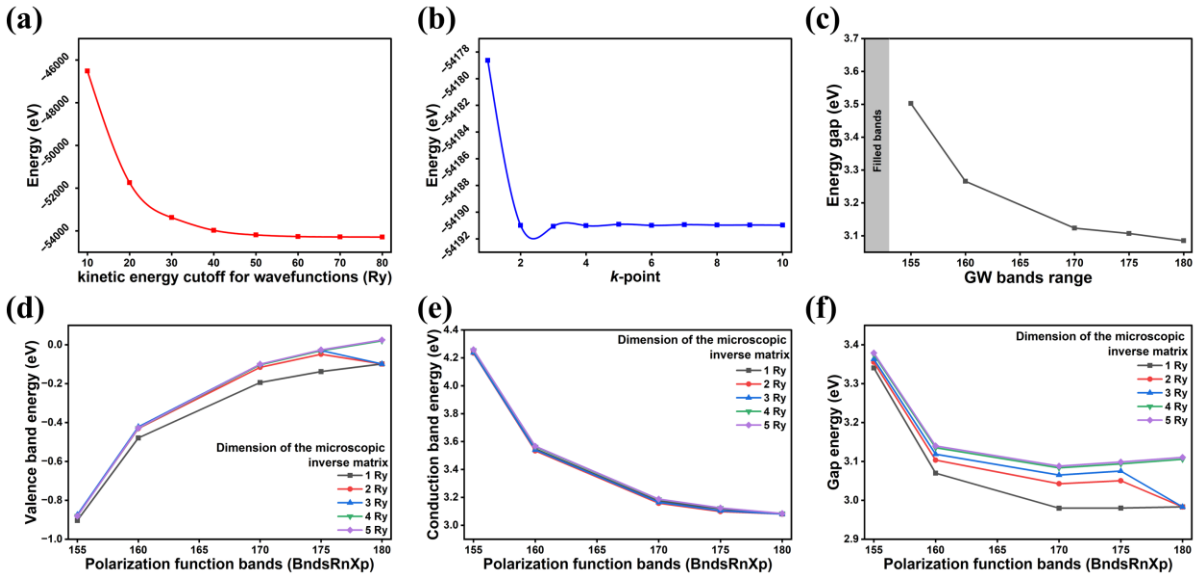

Figure S1: Convergence tests for the SnS/(5,0) BNNT heterostructure: (a) kinetic energy cutoff for wavefunctions and (b) *k*-point sampling at the DFT-GGA level. Convergence with respect to (c) the number of unoccupied states included in the correlation self-energy summation, and (d–f) the number of bands used to construct the RPA response function (BndsRnXp) and the number of dielectric matrix blocks considered for the valence band, conduction band, and band gap energy, respectively.

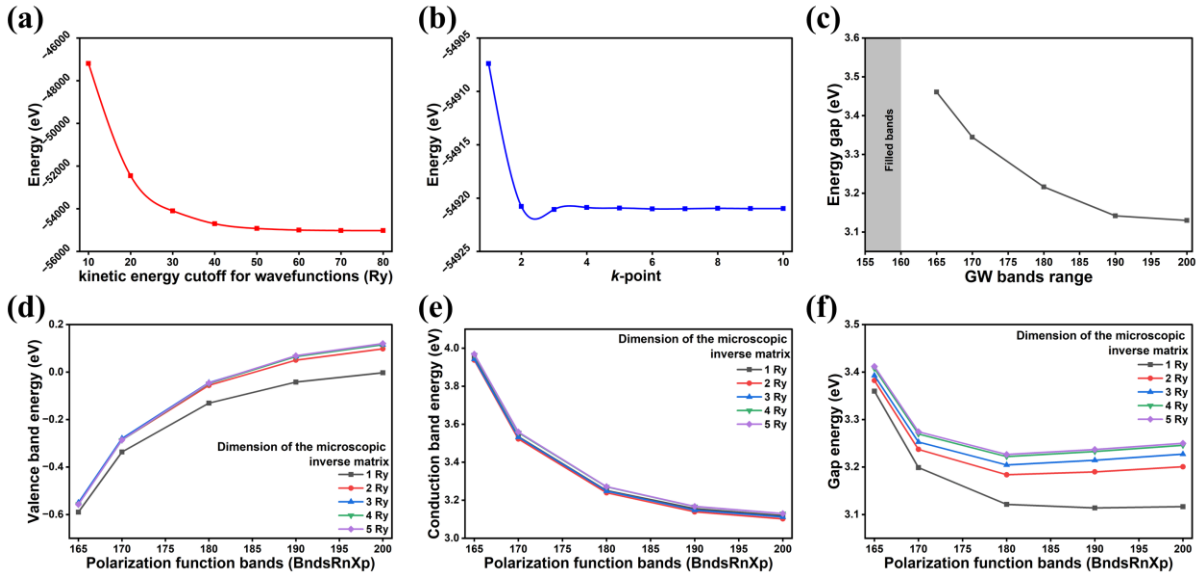

Figure S2: Convergence tests for the SnS/(6,0) BNNT heterostructure: (a) kinetic energy cutoff for wavefunctions and (b) *k*-point sampling at the DFT-GGA level. Convergence with respect to (c) the number of unoccupied states included in the correlation self-energy summation, and (d–f) the number of bands used to construct the RPA response function (BndsRnXp) and the number of dielectric matrix blocks considered for the valence band, conduction band, and band gap energy, respectively.

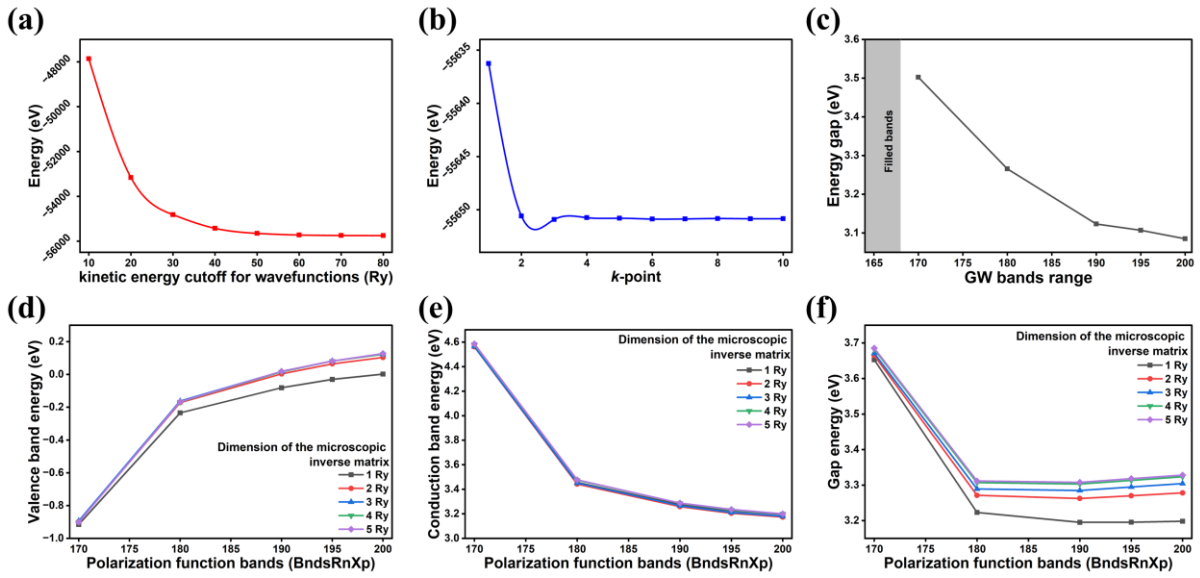

Figure S3: Convergence tests for the SnS/(7,0) BNNT heterostructure: (a) kinetic energy cutoff for wavefunctions and (b) *k*-point sampling at the DFT-GGA level. Convergence with respect to (c) the number of unoccupied states included in the correlation self-energy summation, and (d–f) the number of bands used to construct the RPA response function (BndsRnXp) and the number of dielectric matrix blocks considered for the valence band, conduction band, and band gap energy, respectively.

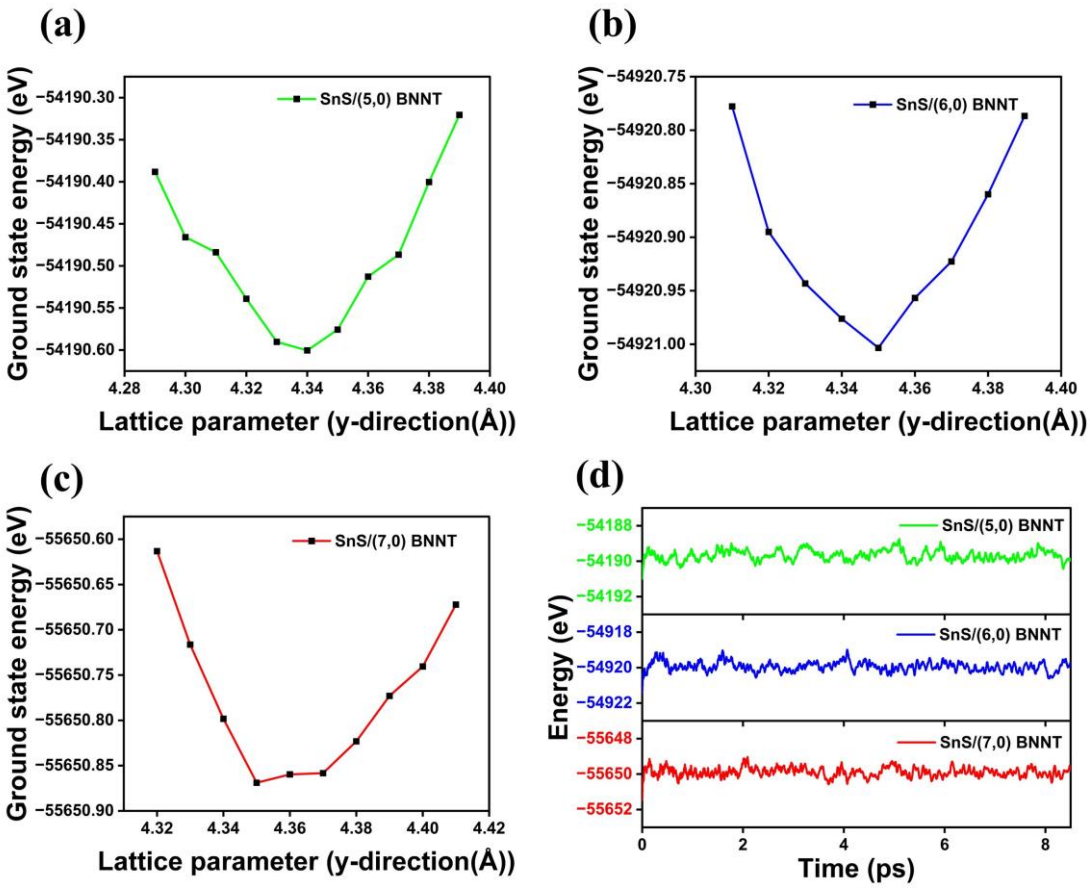

Figure S4: (a-c) Convergence test for lattice parameters vs. ground state energy; (d) AIMD simulation of the SnS/BNNT heterostructures at 300 K.

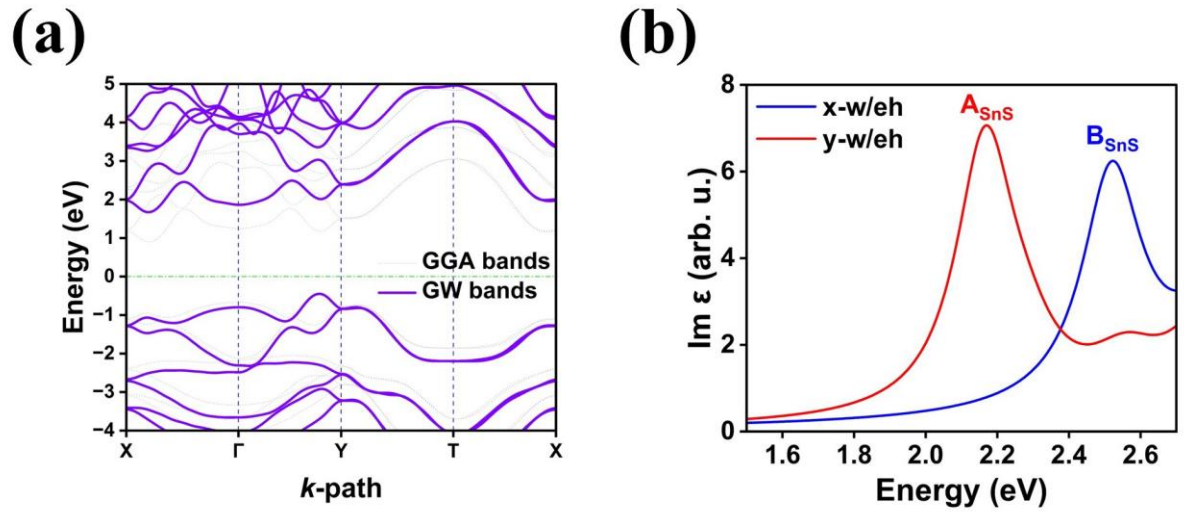

Figure S5: (a) Electronic band structure and (b) optical absorption spectra of SnS monolayer.

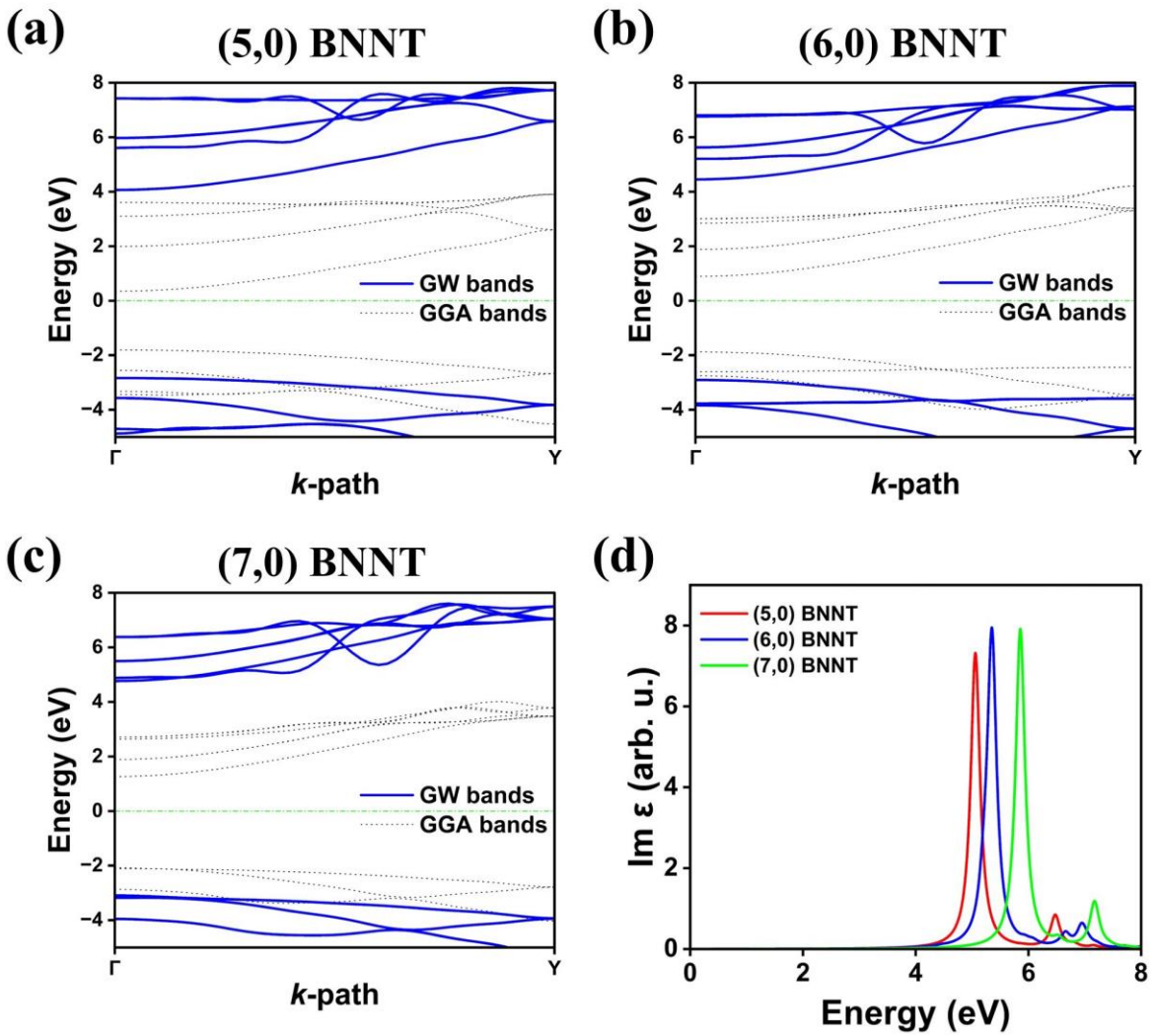

Figure S6: Electronic band structure of (a) (5,0) (b) (6,0), and (c) (7,0) BNNTs; (d) optical absorption spectra of the BNNTs.

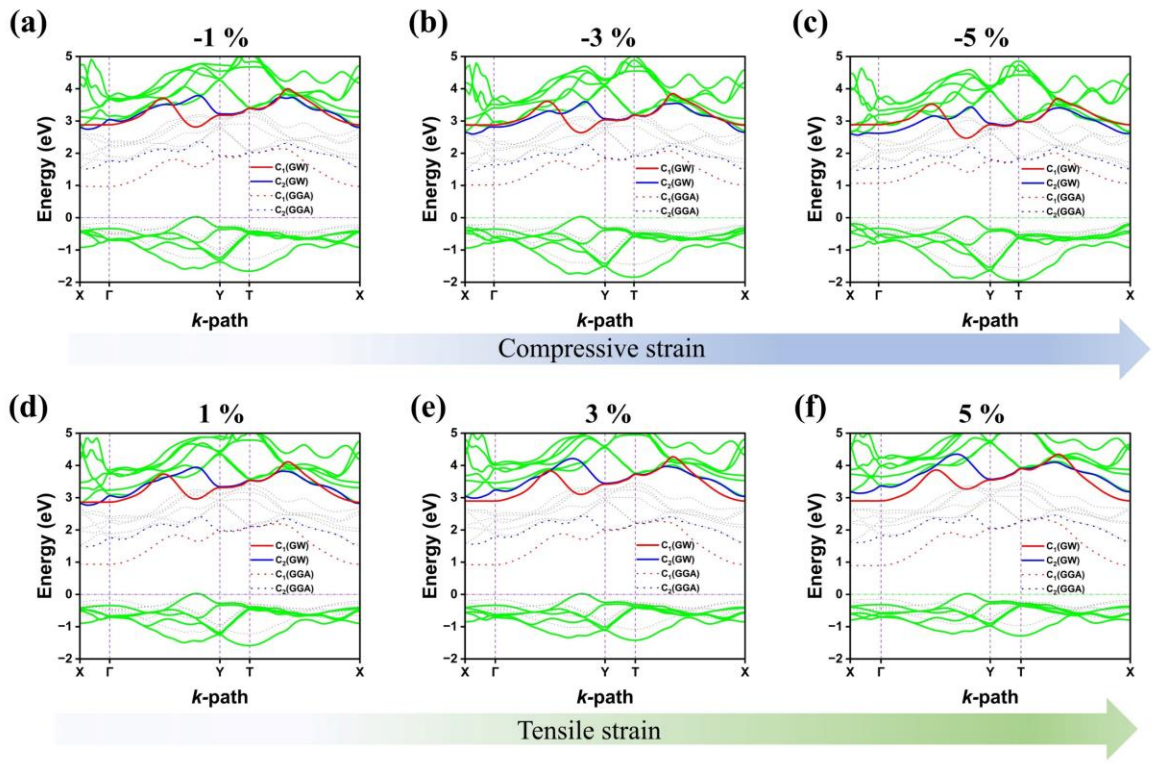

Figure S7: Electronic band structures of the SnS/(5,0) BNNT heterostructure under uniaxial strain applied along the nanotube axis. Panels (a-c) show the band structures under compressive strain of -1%, -3%, and -5%, respectively, while panels (d-f) correspond to tensile strain of +1%, +3%, and +5%.

Table S1: Peak positions of the IDEs under tensile strain.

Strain %	IDEs energies (eV)	No. of IDEs
0 (unstrained)	2.68	1
1%	2.50, 2.56, 2.64, 2.67, 2.70	5
3%	2.48, 2.54, 2.67, 2.70, 2.74, 2.77, 2.80, 2.83	8
5%	2.00, 2.32, 2.36, 2.40, 2.43, 2.48, 2.52, 2.54, 2.57, 2.63	10

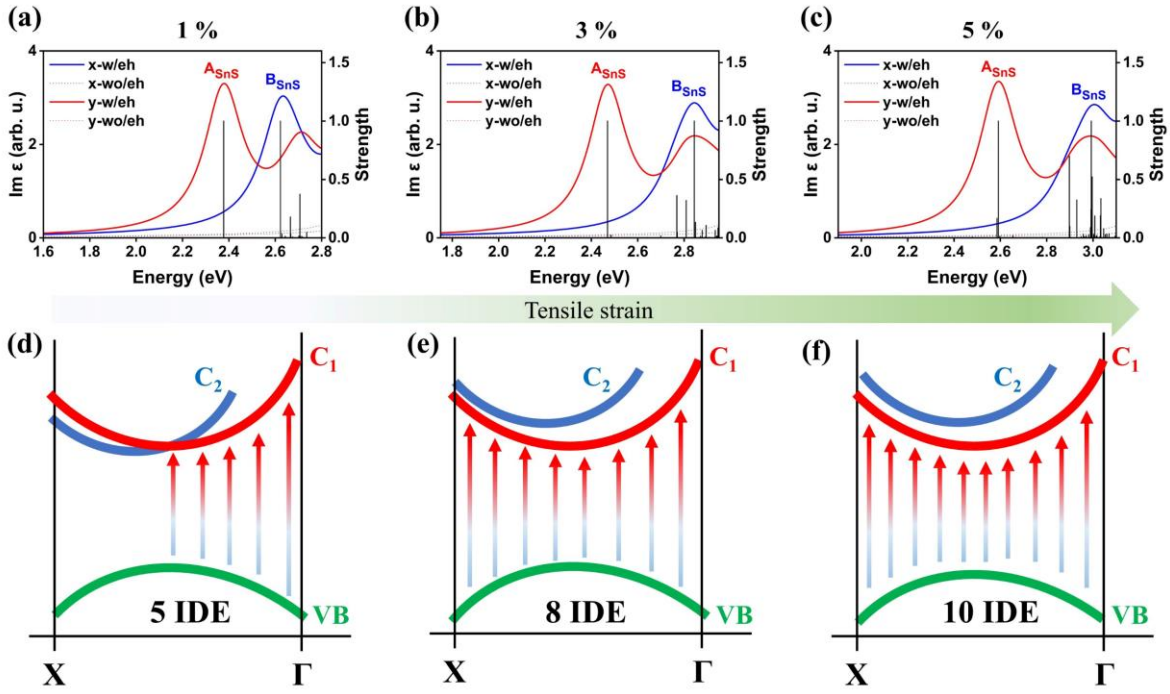

Figure S8: Optical absorption spectra of the SnS/(5,0) BNNT heterostructure under uniaxial tensile strain of (a) 1%, (b) 3%, and (c) 5%. The corresponding schematic illustrations in (d-f) depict the evolution of the C_1 and C_2 conduction bands with increasing tensile strain, highlighting the increase in the number of available IDE transition states across the Γ-X valley.

References

1 P. Giannozzi, S. Baroni, N. Bonini, M. Calandra, R. Car, C. Cavazzoni, D. Ceresoli, G. L. Chiarotti, M. Cococcioni and I. Dabo, *Journal of physics: Condensed matter*, 2009, **21**, 395502.

2 P. Giannozzi, O. Andreussi, T. Brumme, O. Bunau, M. B. Nardelli, M. Calandra, R. Car, C. Cavazzoni, D. Ceresoli and M. Cococcioni, *Journal of physics: Condensed matter*, 2017, **29**, 465901.

3 I. Carnimeo, F. Affinito, S. Baroni, O. Baseggio, L. Bellentani, R. Bertossa, P. D. Delugas, F. F. Ruffino, S. Orlandini and F. Spiga, *J Chem Theory Comput*. 2023, **19(20)**, 6992–7006

4 P. Giannozzi, O. Baseggio, P. Bonfà, D. Brunato, R. Car, I. Carnimeo, C. Cavazzoni, S. De Gironcoli, P. Delugas and F. Ferrari Ruffino, *J Chem Phys*., 2020, **152**, 154105.

5 J. P. Perdew, K. Burke and M. Ernzerhof, *Phys Rev Lett*, 1996, **77**, 3865.

6 D. R. Hamann, *Physical Review B—Condensed Matter and Materials Physics*, 2013, **88**, 085117.

7 V. Barone, M. Casarin, D. Forrer, M. Pavone, M. Sambi and A. Vittadini, *J Comput Chem*, 2009, **30**, 934–939.

8 G. Onida, L. Reining and A. Rubio, *Rev Mod Phys*, 2002, **74**, 601.

9 M. Rohlfing and S. G. Louie, *Phys Rev B*, 2000, **62**, 4927.

10 G. Strinati, *Phys Rev B*, 1984, **29**, 5718.

11 D. Sangalli, A. Ferretti, H. Miranda, C. Attaccalite, I. Marri, E. Cannuccia, P. Melo, M. Marsili, F. Paleari and A. Marrazzo, *Journal of Physics: Condensed Matter*, 2019, **31**, 325902.

12 A. Marini, C. Hogan, M. Grüning and D. Varsano, *Comput Phys Commun*, 2009, **180**, 1392–1403.